A Vector Wiener Filter for Dual-Radionuclide Imaging

Jonathan M. Links, Jerry L. Prince,* *Senior Member, IEEE*, and Sandeep N. Gupta

***Abstract*—The routine use of a single radionuclide for patient imaging in nuclear medicine can be complemented by studies employing two tracers to examine two different processes in a single organ, most frequently by simultaneous imaging of both radionuclides in two different energy windows. In addition, simultaneous transmission/emission imaging with dual-radionuclides has been described, with one radionuclide used for the transmission study and a second for the emission study. There is thus currently considerable interest in dual-radionuclide imaging. A major problem with all dual-radionuclide imaging is the "crosstalk" between the two radionuclides. Such crosstalk frequently occurs, because scattered radiation from the higher energy radionuclide is detected in the lower energy window, and because the lower energy radionuclide may have higher energy emissions which are detected in the higher energy window. We have previously described the use of Fourier-based restoration filtering in single photon emission computed tomography (SPECT) and positron emission tomography (PET) to improve quantitative accuracy by designing a Wiener or other Fourier filter to partially restore the loss of contrast due to scatter and finite spatial resolution effects. We describe here the derivation and initial validation of an extension of such filtering for dual-radionuclide imaging that simultaneously 1) improves contrast in each radionuclide's "direct" image, 2) reduces image noise, and 3) reduces the crosstalk contribution from the other radionuclide. This filter is based on a vector version of the Wiener filter, which is shown to be superior [in the minimum mean square error (MMSE) sense] to the sequential application of separate crosstalk and restoration filters.**

I. Introduction

THE routine use of a single radionuclide for patient imaging in nuclear medicine can be complemented by studies employing two tracers labeled with different radionuclides to examine two different processes in a single organ. Such studies most frequently employ simultaneous imaging of both radionuclides in two different energy windows, yielding perfectly registered image pairs. This approach has been in use for over a decade, for example in parathyroid disease (e.g., [1]), and more recently in liver disease [2], cardiac disease (e.g., [3] and [4]–[7]), and studies of brain perfusion [8]. In addition, simultaneous transmission/emission imaging has been described in single photon emission tomography (SPECT) (e.g., [9] and [10]), with one radionuclide used for the transmission study and a second for the emission study. There is thus currently considerable interest in dual-radionuclide (also known as dual-isotope) imaging.

A major problem with all dual-radionuclide imaging is the "crosstalk" between the two radionuclides. Such crosstalk frequently occurs, because scattered radiation from the higher energy radionuclide is detected in the lower energy window, and because the lower energy radionuclide may have higher energy emissions which are detected in the higher energy window. Depending on the energies of emissions from the two radionuclides, the positions of the energy windows relative to these emissions, and the energy resolution of the imaging system, the crosstalk contribution may be of either lower or higher spatial frequency in character. For example, in the case of Tl-201 and Tc-99m, the crosstalk from Tc-99m into the Tl-201 window is primarily from multiply scattered photons and Pb X-rays from the collimator, and is thus primarily low frequency in character, while the crosstalk from Tl-201 into the Tc-99m window is from both unscattered and scattered photons, and thus contains some higher frequency information [10]. On the other hand, in the case of Tc-99m and I-123, much of the crosstalk is from unscattered photons, because of the close proximity of the two photopeaks and pulse height blurring due to energy resolution effects, and thus may contain significant high frequency information [11].

Crosstalk has been demonstrated to be a major problem in many dual-radionuclide imaging studies. For example, Ivanovic and coworkers [12] used Monte Carlo simulations to demonstrate that the crosstalk component may be as high as 50% for certain brain imaging situations. Weinstein and coworkers [7] and Kiat and coworkers [13] demonstrated similar magnitude effects in myocardial perfusion SPECT. Kiat concluded that the "simultaneous dual-radionuclide protocol should not be used until satisfactory techniques for correction of Tc-99m crosstalk are developed." There is only one published study indicating minimal effects of crosstalk [14]; this study used phantoms with large defects. An accompanying editorial [15] warned of the limited utility of these findings in human SPECT studies.

Most investigators did not propose solutions to the crosstalk problem, but instead sought to minimize the crosstalk con-

Manuscript received April 10, 1995; revised May 31, 1996. This work was supported by the National Institutes of Health under Grant R01-CA32845 and the National Science Foundation under Grant MIP93-50336. The Associate Editor responsible for coordinating the review of this paper and recommending its publication was V. Johnson. *Asterisk indicates corresponding author.*

J. M. Links is with the Department of Environmental Health Sciences and Department of Electrical and Computer Engineering, The Johns Hopkins University School of Public Health, Baltimore, MD 21205 USA.

*J. L. Prince is with the Department of Electrical and Computer Engineering, 105 Barton Hall, Department of Electrical and Computer Engineering, The Johns Hopkins University, 3400 North Charles Street, Baltimore, MD 21218 USA (e-mail: jprince@jhu.edu). He is also with the Department of Radiology, The Johns Hopkins University School of Medicine, Baltimore, MD 21205 USA.

S. N. Gupta is with the Department of Electrical and Computer Engineering, The Johns Hopkins University, Baltimore, MD 21218 USA.

Publisher Item Identifier S 0278-0062(96)07200-X.

tribution (e.g., through the use of asymmetric energy windows; [11]). Investigators interested in simultaneous transmission/emission imaging (e.g., [9] and [10]) have described methods which attempt to reduce crosstalk effects. For example, Frey and coworkers [10] modeled the crosstalk as a contribution to the other window proportional to the direct window image, and empirically obtained proportionality constants (which they referred to as correction factors). In essence, a fraction of each direct window image (determined by the appropriate proportionality constant) was subtracted from the other window, although the exact implementation was more analytically correct than this oversimplified statement. Bailey and coworkers [9] modeled the imaging process as linear, shift-invariant, and wide-sense stationary. They described the crosstalk from the higher energy radionuclide into the lower energy window as the convolution of the higher energy radionuclide's distribution with a crosstalk function (which they referred to as the point spread function for the higher energy radionuclide as seen in the lower energy window). In practice, since the true distribution for the higher energy radionuclide was unknown, an empirically modeled scatter function was convolved with the higher energy window image, and the resulting "crosstalk image" subtracted from the lower energy window image. Knesaurek [16] extended this approach to dual-radionuclide Tl-201/Tc-99m cardiac SPECT. He showed significant improvement in quantification of the distribution of Tl-201 in a cardiac phantom as a result of crosstalk correction. Knesaurek's goal was only to "remove" the crosstalk contribution to each image, resulting in images which were still degraded by direct blur and noise. Presumably, these images could then be corrected by a conventional restoration filter (e.g., [17]–[28]), although this was not proposed by Knesaurek.

We propose a new approach, vector Wiener filtering, that simultaneously considers direct blur, noise, and crosstalk. This approach is based on an extension of the use of two-dimensional (2-D) Fourier filters, usually referred to as image restoration filters, in nuclear medicine. While many different image restoration filters have been described in the general image processing literature (e.g., [29]), the filters used in these nuclear medicine studies were typically based on the measured point spread function (PSF), and its Fourier transform, the modulation transfer function (MTF), and characteristics of the image itself. Such filters seek to minimize the mean-square-error between the filtered image and the original object; a prototypical image restoration filter is the Wiener filter [30]. We here hypothesize that dual-radionuclide SPECT imaging can be conceptualized as a vector imaging problem [31], and that a vector version of the Wiener filter can be used to simultaneously 1) improve contrast in each radionuclide's direct image, 2) reduce image noise, and 3) reduce or eliminate the crosstalk contribution from the other radionuclide. We further hypothesize that our approach is superior (in the MMSE sense) to the sequential application of separate crosstalk and restoration filters. Below, we first present the derivation of the vector Wiener filter (VWF), followed by a theoretical analysis that demonstrates its superiority to sequential crosstalk and restoration filtering. We then consider implementation issues, and present the results of computer simulations.

II. Vector Wiener Filter (VWF)

The Wiener filter for vector-valued images has been explored by several groups within the frameworks of multispectral image restoration [32], multichannel image restoration [33], and multiframe image restoration [34]. An overview of these approaches is provided in [35]. The derivations of the VWF within these papers apply to digital images with multiple values at each pixel. These images are represented by vectors of dimensionality equal to the number of pixels in the image times the number of values at each pixel. By using the standard expression for the linear minimum mean square error (LMMSE) estimate (cf. [29]), a linear algebraic form of the Wiener filter is easily written. Application of the discrete Fourier transform (DFT) operator leads to a discrete Fourier Wiener filter for vector-valued images [33]. In this paper, we derive from first principles a continuous Fourier Wiener filter for vector-valued images. We believe that this derivation and result are more accessible to the medical imaging community than previous discrete derivations and results (cf. [33]), since the final form is similar to the "usual" Wiener filter in standard textbooks (e.g., [30]). The tradeoffs and approximations typically required for practical implementation are therefore more easily discovered from this form of the filter. The derivation follows from the principle of orthogonality, widely used in the derivation of LMMSE solutions [36]. Since we are not concerned with causality in imaging systems, we avoid the difficult issues associated with spectral matrix factorization, which occur in vector time-series implementations of the Wiener filter [37].

A. Notation

We have chosen to use conventional signal processing notation in the following derivation. Here, x and y are the input and output functions, respectively, not independent variables (i.e., they are not spatial locations). Independent variables are represented by t, s, and τ, and represent 2-D locations. The derivation and solution are most conveniently written using matrix notation. In keeping with standard notation, vectors and matrices are indicated with boldface type—e.g., $\mathbf{x}$ and $\mathbf{y}$ are vectors and $\mathbf{H}$ and $\mathbf{G}$ are matrices. Matrices containing Fourier transforms are denoted using script type—e.g., $\mathcal{S}$, $\mathcal{G}$, and $\mathcal{H}$. Since our result is derived on the continuum, images are not viewed as finite vectors, but as functions on the plane.

B. Observation Model

We model the dual-radionuclide imaging process as a linear, shift-invariant, multi-input/multi-output system [31]. The two true radionuclide distributions x_1 and x_2 are blurred by the imaging system's impulse response functions h_{ij}, $i, j = 1, 2$, and noise is added, producing the observations y_1 and y_2 as follows:

$$y_1 = h_{11} * x_1 + h_{12} * x_2 + n_1 \tag{1a}$$

$$y_2 = h_{21} * x_1 + h_{22} * x_2 + n_2 \tag{1b}$$

where $*$ denotes convolution. Here, y_1 and y_2 represent observations corresponding to the true distributions x_1 and x_2 of

the same dimensionality. Thus, if y_1 and y_2 are 2-D projection data, x_1 and x_2 are the corresponding 2-D true distributions; if y_1 and y_2 are three-dimensional (3-D) reconstructed data sets, x_1 and x_2 are the corresponding 3-D true distributions. Impulse response h_{ij} represents the response to radionuclide j in energy window i. When $i = j$, h_{ij} produces direct blurring, and when $i \neq j$, h_{ij} produces crosstalk blurring. Although one can expect a noise contribution resulting from each source, we make the simplifying assumption that these independent noise contributions can be combined and modeled as a single noise contribution to each window.

The cross-blurring functions represent the contamination of direct emissions received in one window by emissions from the other radionuclide. In practice, the higher energy radionuclide significantly contaminates the lower energy window (usually via Compton scattering), but the reverse is not always true. In other words, one of the cross-blurring functions may be of much lower magnitude. However, we treat the more general case here for deriving the relations by not placing any restrictions on these functions.

From the observed y_i and knowledge of h_{ij}, we wish to obtain the best estimates of x_j, which we denote as $\hat{x}_j$. We find that these estimates are given by

$$\hat{x}_1 = g_{11} * y_1 + g_{21} * y_2 \tag{2a}$$

$$\hat{x}_2 = g_{12} * y_1 + g_{22} * y_2 \tag{2b}$$

where g_{ij} are the optimal (vector) Wiener filter impulse responses prescribed by the derivation given below. In keeping with the previous notation, g_{ij} denotes the filter applied to the ith observation (energy window) that contributes to the estimate of the jth source (radionuclide distribution). It is important to note that, in general, both observed images contribute toward both estimates. This particular mathematical formulation provides the basis for the approach described here.

It is convenient to represent the observation and filtering processes with vector notation. Letting $\mathbf{y} = [y_1\ y_2]^{\mathrm{T}}$, $\mathbf{x} = [x_1\ x_2]^{\mathrm{T}}$, and $\mathbf{n} = [n_1\ n_2]^{\mathrm{T}}$, (1) can be written as

$$\mathbf{y} = \mathbf{H} * \mathbf{x} + \mathbf{n}. \tag{3}$$

Here, $\mathbf{H}$ is a matrix of impulse responses given by

$$\mathbf{H} = \begin{bmatrix} h_{11} & h_{12} \\ h_{21} & h_{22} \end{bmatrix}$$

and $*$ represents vector convolution, which is defined by

$$(\mathbf{H} * \mathbf{x})_i = \sum_{j=1}^{2} h_{ij} * x_j.$$

The filtering process given by (2) can similarly be written with vector notation as

$$\hat{\mathbf{x}} = \mathbf{G}^{\mathrm{T}} * \mathbf{y} \tag{4}$$

where $\hat{\mathbf{x}} = [\hat{x}_1\ \hat{x}_2]^{\mathrm{T}}$ and

$$\mathbf{G} = \begin{bmatrix} g_{11} & g_{12} \\ g_{21} & g_{22} \end{bmatrix}. \tag{5}$$

With the observation and filtering processes written in this form, we can now derive $\mathbf{G}$.

C. Wiener Filter Derivation

A *Wiener filter* is the LMMSE estimator of a wide-sense stationary random process given observations of that random process over an infinite interval [36]; it is optimal in that sense. A VWF extends this result to the estimation of vector-valued random processes. The LMMSE estimator impulse response functions g_{ij} are derived using the orthogonality condition [36], which states that the estimation error is orthogonal to the data. This condition can be written as

$$E[(\mathbf{x}(t+\tau) - \hat{\mathbf{x}}(t+\tau))\mathbf{y}^{\mathrm{T}}(t)] = \mathbf{0}, \quad \forall t, \tau \tag{6}$$

where $E[\cdot]$ denotes expectation. Using (4) and (6) it can shown that $\mathbf{G}$ must satisfy

$$\mathbf{R}_{\mathbf{xy}}(\tau) = \mathbf{G}^{\mathrm{T}}(\tau) * \mathbf{R}_{\mathbf{yy}}(\tau), \quad \forall \tau \tag{7}$$

where the autocorrelation matrices $\mathbf{R}$ are given by

$$\mathbf{R}_{\mathbf{xy}}(\tau) = \begin{bmatrix} R_{x_1y_1}(\tau) & R_{x_1y_2}(\tau) \\ R_{x_2y_1}(\tau) & R_{x_2y_2}(\tau) \end{bmatrix} \tag{8}$$

where $R_{x_my_n}(\tau) = E[x_m(t+\tau)y_n(t)]$ and

$$\mathbf{R}_{\mathbf{yy}}(\tau) = \begin{bmatrix} R_{y_1y_1}(\tau) & R_{y_1y_2}(\tau) \\ R_{y_2y_1}(\tau) & R_{y_2y_2}(\tau) \end{bmatrix} \tag{9}$$

where $R_{y_my_n}(\tau) = E[y_m(t+\tau)y_n(t)]$. Taking the Fourier transform of both sides, using the convolution theorem, and rearranging yields

$$\mathcal{G}^{\mathrm{T}}(f) = \mathcal{S}_{\mathbf{xy}}(f)\mathcal{S}_{\mathbf{yy}}^{-1}(f), \quad \forall f \tag{10}$$

where f is the (2-D) frequency variable corresponding to τ and $\mathcal{S}_{\mathbf{xy}}$ and $\mathcal{S}_{\mathbf{yy}}$ are the (element-by-element) Fourier transforms of $\mathbf{R}_{\mathbf{xy}}$ and $\mathbf{R}_{\mathbf{yy}}$, respectively. Note that this is a matrix equation where superscript -1 represents matrix inverse.

Equation (10) is the fundamental form of the VWF. To complete the derivation, we now use the observation equation (3) to find explicit expressions for $\mathcal{S}_{\mathbf{xy}}$ and $\mathcal{S}_{\mathbf{yy}}$. Using (3) and the assumption that $\mathbf{x}$ and $\mathbf{n}$ are uncorrelated, it can be shown that

$$\mathbf{R}_{\mathbf{xy}}(\tau) = \mathbf{R}_{\mathbf{xx}}(\tau) * \mathbf{H}^{\mathrm{T}}(-\tau) \tag{11}$$

where $\mathbf{R}_{\mathbf{xx}}$ is defined analogously to $\mathbf{R}_{\mathbf{yy}}$ above. Taking Fourier transforms and using the convolution theorem yields

$$\mathcal{S}_{\mathbf{xy}}(f) = \mathcal{S}_{\mathbf{xx}}(f)\mathcal{H}^{\mathrm{H}}(f) \tag{12}$$

where the superscript H stands for conjugate (or Hermitian) transpose. Using a similar procedure, it can be shown that

$$\mathbf{R}_{\mathbf{yy}}(\tau) = \mathbf{H}(\tau) * \mathbf{R}_{\mathbf{xx}}(\tau) * \mathbf{H}^{\mathrm{T}}(-\tau) + \mathbf{R}_{\mathbf{nn}}(\tau) \tag{13}$$

and

$$\mathcal{S}_{\mathbf{yy}}(f) = \mathcal{H}(f)\mathcal{S}_{\mathbf{xx}}(f)\mathcal{H}^{\mathrm{H}}(f) + \mathcal{S}_{\mathbf{nn}}(f). \tag{14}$$

Substituting (12) and (14) into (10) yields the VWF

$$\mathcal{G}^{\mathrm{T}}(f) = \mathcal{S}_{\mathbf{xx}}(f)\mathcal{H}^{\mathrm{H}}(f)[\mathcal{H}(f)\mathcal{S}_{\mathbf{xx}}(f)\mathcal{H}^{\mathrm{H}}(f) + \mathcal{S}_{\mathbf{nn}}(f)]^{-1}. \tag{15}$$

The quantity $\mathcal{G}^{\mathrm{T}}(f)$ is a matrix of Fourier transforms, which upon inverse Fourier transformation yields $\mathbf{G}^{\mathrm{T}}$, the matrix of the Wiener filter impulse responses.

The form of $\mathcal{G}$ in (15) permits the comparison of the VWF with the conventional (scalar) Wiener filter. In nuclear medicine, it is common to write the scalar Wiener filter as

$$G = H^{-1}\frac{|H|^2}{|H|^2 + S_n/S_x}$$

where the notation is the scalar analog of our vector notation. Since $|H|^2 = HH^*$ (where superscript $*$ denotes the complex conjugate), this equation can be rearranged as

$$G = S_x H^*[HS_xH^* + S_n]^{-1}.$$

Comparison of this equation with (15) emphasizes the essentially equivalent form of the scalar and VWF's. This structural similarity facilitated our understanding and implementation of the VWF.

D. A Comparison to Sequential Filtering

The simultaneous consideration of direct blur, crosstalk, and noise produces a Wiener filtered image with a resultant mean-square-error which is lower than that achievable by the sequential application of a filter which only addresses crosstalk (e.g., such as that described in [16]) followed by a conventional (single-radionuclide, scalar) filter (such as that described in [26]). Since this is an important point that distinguishes these approaches, we now provide a theoretical argument which justifies this conclusion.

Ignoring noise, our observation model of (3) is $\mathbf{y} = \mathbf{H} * \mathbf{x}$, which in the Fourier domain can be written $\mathcal{Y} = \mathcal{H}\mathcal{X}$, where $\mathcal{H}\mathcal{X}$ is a matrix multiplication. Then, if $\mathcal{H}$ is invertible, one could form $\mathcal{X} = \mathcal{H}^{-1}\mathcal{Y}$. To get the direct blurred version of $\mathbf{x}$ back again (in the Fourier domain), we just multiply the first and second elements of $\mathcal{X}$ by the Fourier transforms of h_{11} and h_{22}, respectively. This is equivalent to premultiplying $\mathcal{X}$ by a diagonal matrix $\mathcal{H}_d$ having only the diagonal elements of $\mathcal{H}$. It can be shown that the method of Knesaurek [16], which gives an estimate of the direct blurred observations, is exactly (in the Fourier domain)

$$\mathcal{K} = \mathcal{H}_d\mathcal{H}^{-1}\mathcal{Y}. \tag{16}$$

Now, suppose one substitutes the actual observation equation (3) into (16). This yields

$$\mathcal{K} = \mathcal{H}_d\mathcal{X} + \mathcal{H}_d\mathcal{H}^{-1}\mathcal{N}.$$

This shows that the $\mathcal{X}$'s uncouple (because $\mathcal{H}_d$ is diagonal) but the noise components couple (because $\mathcal{H}_d\mathcal{H}^{-1}$ is not diagonal). Writing separate scalar equations in real-space gives

$$k_1 = h_{11} * x_1 + a * n_1 + b * n_2$$
$$k_2 = h_{22} * x_2 + c * n_1 + d * n_2$$

where a, b, c, d are functions determined by taking the inverse Fourier transform of $\mathcal{H}_d\mathcal{H}^{-1}$. This could be written as

$$k_1 = h_{11} * x_1 + n_3$$
$$k_2 = h_{22} * x_2 + n_4$$

which, on the surface, looks suitable for application of separate scalar Wiener filters. However, three things are wrong with this approach.

1) The first filter can involve only $\mathcal{S}_{x1x1}$, the power spectral density of x_1; the second involves only x_2. Therefore, any correlation between x_1 and x_2 cannot be accounted for in this approach.
2) In this approach, n_3 and n_4 are implicitly treated as uncorrelated (because of the use of separate scalar filters). However, since n_1 and n_2 contribute to both n_3 and n_4, n_3 and n_4 must be correlated.
3) n_3 and n_4 are no longer white noise processes, since they have incurred a convolution during the Knesaurek transformation. Any attempt to whiten each noise component separately before filtering ignores their inherent correlation. Whitening the two noise components simultaneously can only be accomplished by "undoing" the Knesaurek transformation; then the optimal filter is ours.

In summary, in the sequential filtering approach, there is no way to model the correlation of x_1 and x_2. High correlation between x_1 and x_2 is expected to frequently occur, particularly in brain imaging studies. There is no way to model the correlation of n_3 and n_4 caused by the Knesaurek transformation. Finally, the nonwhiteness of n_3 and n_4 would have to be first undone before applying a standard Wiener filter. Therefore, the sequential application of Knesaurek's method followed by two scalar Wiener filters is suboptimal—i.e., produces a larger mean square error—and is not equivalent to our vector Wiener approach.

E. Implementation

In practice, (15) is directly used to yield the Fourier transforms of the four filter impulse responses g_{ij} which, together, form the VWF. Computation of $\mathcal{G}$ requires knowledge of the four impulse response functions, h_{ij}, and the spectral density matrices $\mathcal{S}_{\mathbf{xx}}$ and $\mathcal{S}_{\mathbf{nn}}$.

The impulse response functions are obtained by direct measurements as follows. Two points sources, each containing one of the two radionuclides, are made by placing a small drop of liquid containing the radioactivity in the end of a capillary tube. Four images are acquired, representing the two radionuclides and the two energy windows; these yield h_{ij}. In practice, the point sources should be placed in a scattering phantom whose geometry mimics the clinical imaging situation of interest—e.g., head or thorax.

The spectral density matrices $\mathcal{S}_{\mathbf{xx}}$ and $\mathcal{S}_{\mathbf{nn}}$ are estimated using a modification of an approach used in conventional Wiener filtering [26]. First, we estimate $\mathcal{S}_{\mathbf{yy}}$ using the Welch averaged periodogram method [38], [39]. Each image is treated as nine overlapping subimages, and their periodograms are computed; the estimate of $\mathcal{S}_{\mathbf{yy}}$ is the average of these periodograms. Next, we assume that the noise components are uncorrelated with each other and that each noise component is white; this implies that $\mathcal{S}_{\mathbf{nn}}$ is a diagonal matrix. The intensity of each noise component is estimated by averaging the diagonal terms in $\mathcal{S}_{\mathbf{yy}}$ at frequencies above that at which H_{11} is less than 0.05.

To estimate $\mathcal{S}_{\mathbf{xx}}$ we rearrange (14) as follows:

$$\mathcal{S}_{\mathbf{xx}}(f) = \mathcal{H}^{-1}(f)(\mathcal{S}_{\mathbf{yy}}(f) - \mathcal{S}_{\mathbf{nn}}(f))(\mathcal{H}^{\mathrm{H}}(f))^{-1} \quad (17)$$

where the estimated power spectral densities $\mathcal{S}_{\mathbf{yy}}$ and $\mathcal{S}_{\mathbf{nn}}$ are used. This equation is ill-posed, since the calculation of $\mathcal{H}^{-1}$ can be numerically ill-conditioned. We use a simple regularization procedure in which the determinant of $\mathcal{H}$ in the cofactor expansion of $\mathcal{H}^{-1}$ is not allowed to be less than 0.01.

The actual restoration process can be implemented either in real space or Fourier space. The real space implementation uses the filter impulse responses g_{ij}, obtained by inverse Fourier transformation of $\mathcal{G}$, and directly calculates (2). The Fourier space implementation takes the Fourier transforms of y_i, denoted Y_i, and calculates the Fourier transforms of $\hat{x}_j$, denoted $\hat{X}_j$, using [cf. (2)]

$$\hat{X}_1 = G_{11}Y_1 + G_{21}Y_2 \quad (18a)$$

$$\hat{X}_2 = G_{12}Y_1 + G_{22}Y_2. \quad (18b)$$

The estimates $\hat{x}_j$ are then obtained through inverse Fourier transformation.

III. Computer Simulations

Here, we present preliminary results from the 2-D shift-invariant implementation of this filter, using simulated data. An initial implementation of the approach was performed using MATLAB (The MathWorks, Inc.) on a Silicon Graphics Indigo-2 workstation. Below, we present computer simulations using both regular-shaped objects and realistic brain data from actual magnetic resonance imaging (MRI) data. To get a quantitative measure of the errors, we define the percentage root-mean-square (%rms) error as

$$\%\text{rms} = \frac{\sqrt{\frac{\sum (T-E)^2}{N}}}{\sqrt{\frac{\sum T^2}{N}}} \times 100$$

where

- T original, true image pixel value;
- E estimated image (either observed or filtered) pixel value;
- N number of pixels in a region-of-interest (ROI) for which the %rms error is calculated.

A. "Pillbox" Images

In this illustrative example two 256 by 256-pixel "pillbox" images shown in Fig. 1(a) and (b) were used as the sources x_1 and x_2 respectively. The boxes were 32 by 32 pixels in size, 10 in each image. In x_1 the boxes had pixel values of 100 with a background of zero, and in x_2 they had pixel values of zero, with a background of 100. There were ten boxes in each image, eight at nonoverlapping locations and two at locations that overlapped boxes in the other image. The direct blur impulse response functions were 7 by 7 pixels with values 1.0/96 in all except the central pixel, which had the value 0.5. The direct blur impulse responses each added up to one. The cross blur impulse response function h_{12} was a 7 by 7-pixel uniform blur, with each pixel having the value 0.5*(1/49). The cross blur impulse response function h_{21} was a 3 by 3-pixel uniform blur, with each pixel having the value 0.5*(1/9). The cross blur impulse responses each added up to 1/2. Zero-mean, white, Gaussian noise with variance 25 was added. The observations y_1 and y_2 are shown in Fig. 1(c) and (d), respectively; the %rms error between these observations and the truth is 116.2% and 22.6%, respectively. The estimates $\hat{x}_1$ and $\hat{x}_2$ are shown in Fig. 1(e) and (f), respectively; the percent mean square error between these estimates and the truth is 17.7% and 8.1%, respectively. All %rms figures for this simulation were calculated over the entire image.

This example demonstrates the VWF's capability to simultaneously reduce crosstalk, blur, and noise. The significant numerical improvement in the %rms figures is bolstered by visual inspection of Fig. 1. First, we note that the strong crosstalk present in the observations is virtually absent in the estimates. (Small ghost-like outlines of the boxes from Radionuclide 1 are evident in (f) if one looks carefully). Such crosstalk removal is not always possible, however; it depends in large part on the relationships between the direct blur and cross blur impulse responses. Second, we note that the box edges are much crisper in the estimates than in the observations.

B. Human Brain Simulations

We created realistic simulated brain images which incorporated direct blur, crosstalk, and noise. These simulations were based on actual MRI human data, utilizing an approach we have previously described [40]. To summarize, MRI scans were acquired on a 1.5 T scanner, with a "spoiled grass" (SPGR) pulse sequence (TR = 65, TE = 5, flip angle = 45, NEX = 2). The resulting data sets had 64 slices (1.5 mm spacing), with each slice represented by a 256×256 matrix (0.94 mm/pixel). These images were segmented into gray matter, white matter, and cerebrospinal fluid by fitting the observed gray scale histogram with three Gaussian distributions that minimized the cumulative error. A 3-by-3 median filter was run on the result to reduce outliers.

In the simulations shown here (cf. [8], [11]), gray matter was assigned a value of 100, white matter a value of 25, and cerebrospinal fluid a value of zero for radionuclide 1. Gray matter was assigned a value of 25, white matter a value of six, and cerebrospinal fluid a value of zero for radionuclide 2. Radionuclide 1 was a simulation of Tc-99m; radionuclide 2 was a simulation of I-123. In radionuclide 2's image, the head of the caudate on the viewer's right was assigned a value of 37.5. The two source images are shown in Fig. 2(a) and (b). Actual point spread functions from a Picker Prism 3000 SPECT scanner (energy resolution 9.7%) were used to model direct blur and crosstalk. Measurements were in air, in the center of the scanner, and normalized per mCi. Normalization resulted in crosstalk functions whose areas reflected quantitative crosstalk fractions. Measurements were obtained from ramp-filtered reconstructed images of point sources of Tc-99m and I-123, utilizing a 15% symmetric window for both Tc-99m and I-123. This resulted in two direct functions and two crosstalk functions [11], which were

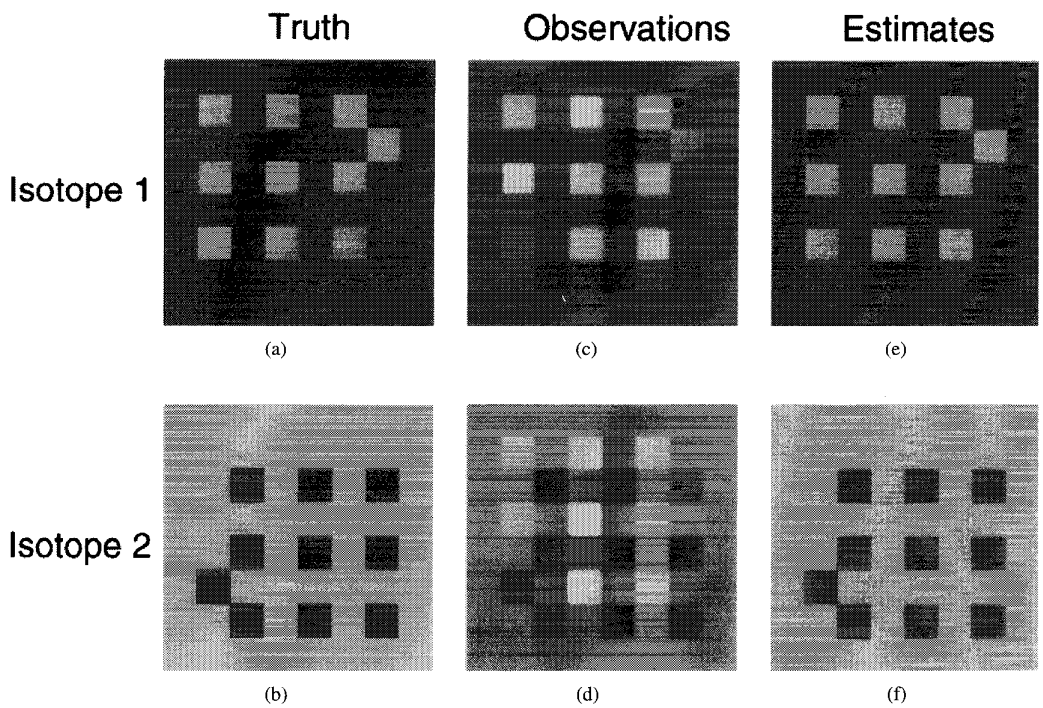

Fig. 1. Pillbox image simulation: (a) x_1, (b) x_2,(c) y_1, (d) y_2, (e) $\hat{x}_1$, and (f) $\hat{x}_2$.

used to produce the simulated observed data. The I-123 to Tc-99m crosstalk function had an area 1/4 that of the direct Tc-99m impulse response function; the Tc-99m to I-123 crosstalk function had an area 1/20 that of the direct I-123 impulse response function. Gaussian noise was added to each image. The variance was 64 for radionuclide 1's image and 16 for radionuclide 2's image. The resulting observed images are shown in Fig. 2(c) and (d). Note that in Fig. 2(c)–(h) the background has been set to zero for improved visualization of the brain.

We performed two different types of crosstalk correction and Wiener filtering. First, we performed the vector Wiener filtering described here. Second, for comparison with the best available published approach, we performed sequential crosstalk correction with Knesaurek's method [16] followed by conventional (scalar) Wiener filtering on each radionuclide's image. The filtered images are shown in Fig. 2(e)–(h).

As shown in Fig. 2(c) and (d), our simulation of the SPECT imaging process indicates significant reduction in resolution, significant noise, and modest crosstalk. The sequential application of Knesaurek's crosstalk correction and scalar Wiener filtering ("K + WF"; Fig. 2(e) and (f)) results in images with significantly increased contrast and reduced noise compared with the observations. The use of our VWF [Fig. 2(g) and (h)] produces further increases in contrast and resolution. Note, for example, the better delineation of the caudate heads, and the more accurate shape and apparent thickness of the cortex in Fig. 2(g) and (h) compared with either the observations (Fig. 2(c) and (d)) or the images after "K + WF" filtering [Fig. 2(e) and (f)]. The improvement within the caudate head is further demonstrated in Fig. 3, where the grayscale values of each image along a row passing through the caudate heads is plotted. This plot clearly shows the significant reduction in noise and increase in quantitative recovery possible with Wiener filtering, with better recovery for the VWF than for "K + WF" filtering.

TABLE I
HUMAN BRAIN SIMULATIONS: %RMS ERROR

ROI		"Radionuclide 1"	"Radionuclide 2"
Image	Observed	61%	70%
	K + WF	55%	55%
	VWF	52%	54%
Brain	Observed	53%	53%
	K + WF	45%	46%
	VWF	43%	43%
Caudate Head	Observed	50%	55%
	K + WF	37%	38%
	VWF	24%	33%

In Table I we report the %rms error for three ROI's: 1) the whole image, 2) the brain, and 3) a 5×5–pixel box within the caudate head. Within the whole image or the brain, there is a modest reduction in %rms error with either filtering approach, the VWF being slightly better. Within the caudate head, there is a substantial reduction in %rms error—roughly a 30% reduction with Knesaurek followed by scalar Wiener filtering, and roughly a 48% reduction with vector Wiener filtering. Since brain SPECT images are frequently interpreted with region-of-interest analysis, such reductions are important, and the difference between "K + WF" filtering and vector Wiener filtering is significant.

In Fig. 4, we show the magnitudes of the four filters G_{ij} that were used to produce the images in Fig. 2(g) and (h). These one-dimensional (1-D) plots of the filters' magnitudes

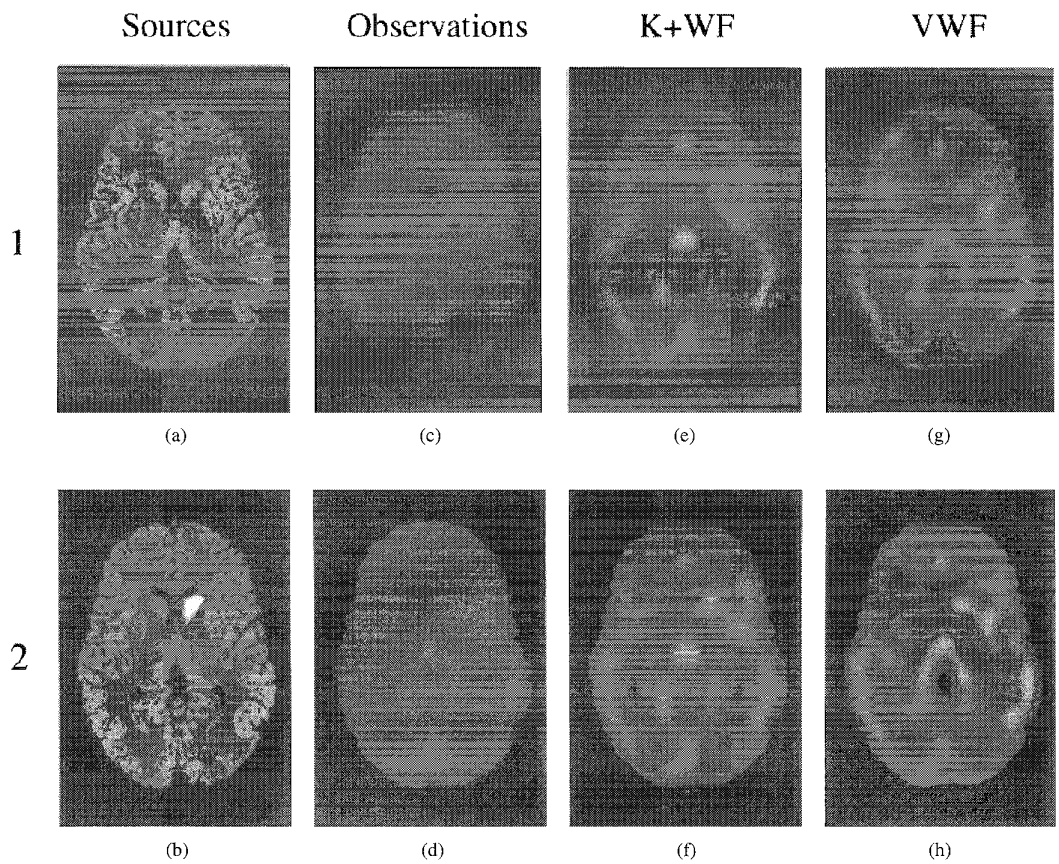

Fig. 2. Human brain simulation: (a) x_1, (b) x_2,(c) y_1, (d) y_2, Knesaurek followed by Wiener filter (K + WF) estimates (e) $\hat{x}_1$, (f) $\hat{x}_2$, and VWF estimates (g) $\hat{x}_1$, and (h) $\hat{x}_2$.

were obtained by averaging a given filter's values at each radial frequency. The two "direct" filters, G_{11} and G_{22}, have an appearance similar to that of conventional Wiener filters: an upslope for recovery followed by a roll-off for noise reduction. The two "cross" filters, G_{12} and G_{21}, have an unusual double-peaked appearance. It is worth noting that the notch frequency is 10 for both G_{12} and G_{21}; this corresponds to the large peak in both G_{11} and G_{22}. The notch in G_{11} corresponds to the first peak in G_{12} and G_{21}. A complete intuitive understanding of the detailed shapes of these four filters would require careful examination of the complex interactions between $\mathcal{H}_{ij}$, $\mathcal{S}_{\mathbf{xx}}$, and $\mathcal{S}_{\mathbf{nn}}$. However, simple inspection of the filters in this figure highlights their interplay in addressing the multichannel properties of the dual-radionuclide imaging situation.

IV. Discussion

Dual-radionuclide imaging is currently receiving renewed attention in nuclear medicine. It offers a powerful approach to the simultaneous imaging of two different physiologic functions, producing images in perfect registration in a clinically useful time. It also offers the possibility of providing registered transmission images for use in attenuation correction in SPECT. However, the use of two simultaneous radionuclides requires correction for crosstalk.

Several groups have previously described the use of Wiener or other Fourier restoration filtering in simultaneously improving image contrast and reducing noise. We have argued that such filtering improves contrast through scatter compensation, and that such compensation is due to repositioning of events, rather than their elimination through subtraction [41]. We now have described a significant extension of these previous efforts through derivation of a new filter formulation, the VWF, and its initial validation in computer simulations. Our approach also builds on convolution-based crosstalk correction schemes previously described by others (e.g., [9] and [16]), and is the analytic combination of restoration filtering and convolution-based crosstalk correction. It has the major advantage of simultaneously considering the three major sources of image degradation: direct blur, crosstalk, and noise. In doing so, the VWF provides a MMSE optimized result.

Inspection of the images in Section III demonstrates improved contrast and reduced noise. The quantitative analyses demonstrate the reduction in root-mean-square (rms) error achievable with such filtering, and its superiority to crosstalk correction followed by conventional Wiener filtering. This reduction in error is due to a combination of signal recovery and noise reduction, although it is difficult to quantify each contribution separately. Inspection of the images also shows a change in noise texture, in that the noise power has shifted

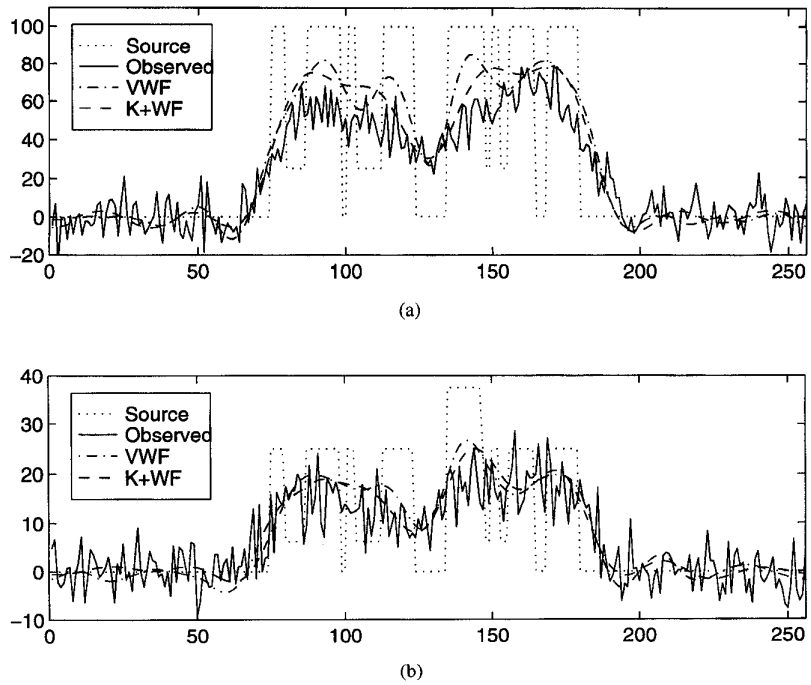

Fig. 3. Human brain simulation. Plots showing the gray scale values from the images of Fig. 2 along a row passing through the caudate. (a) Isotope 1; (b) Isotope 2 (containing the hot spot).

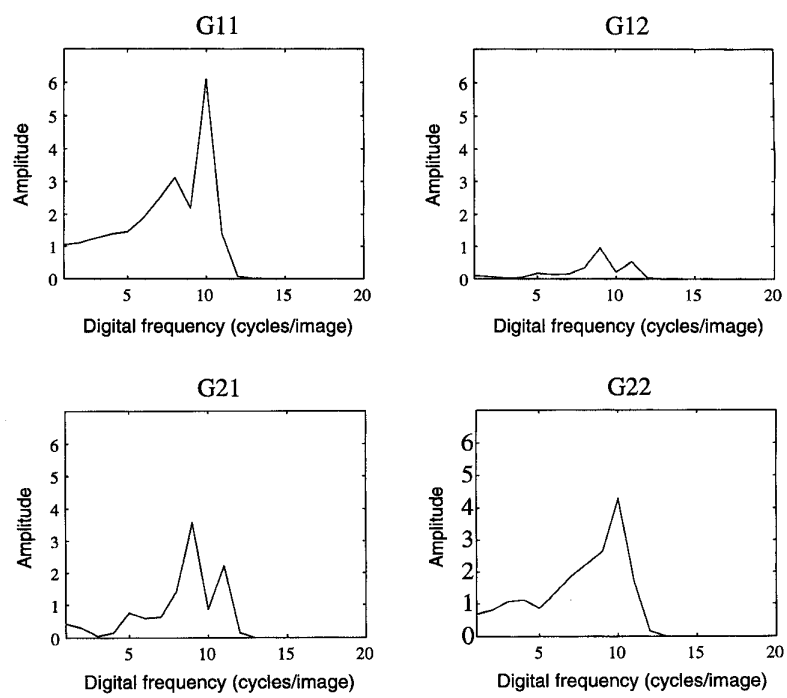

Fig. 4. Plots showing the amplitudes of the four filters $\mathcal{G}_{ij}$ as a function of radial frequency.

to lower frequencies. The noise texture is thus "blob-like" in character. This is a common occurrence with Wiener filtering. We have previously shown that this change in noise texture does not adversely affect quantitative accuracy (as reflected in region-of-interest analysis), and that high frequency noise is reduced (as reflected in pixel-by-pixel noise analysis) [28].

A critical issue requiring further study is the practical approach to full characterization of the two crosstalk functions

in a shift-variant system. In such a system, spatially varying h_{ij} would have to be used. While the convolution operations in (2) could be performed through numerical integration in such a situation, the Fourier-based derivation of the filter impulse responses would not be possible. Although it is important to work toward a shift-variant version, we note that the current assumption of shift-invariance used in Wiener filtering appears sufficiently adequate to produce significant improvements (e.g., [16], [26], [28]). A further issue which has been only partially addressed in the literature (e.g., [12]) is the dependence of the crosstalk functions on the specific windows used. Complete validation of our approach and its assumptions will require more comprehensive computer simulations, actual phantom experiments, and animal experiments. These latter will be particularly important in modeling the complex attenuating environment (including scattering) in clinical imaging situations, particularly myocardial perfusion SPECT [15].

In theory, vector Wiener filtering may be applied at either the projection or reconstructed image level. The advantage of filtering projection data is that we can include variable distances from the detector/collimator to the center of the organ of interest, variable signal-to-noise ratios, and a better model of noise. The "danger" of projection filtering is that the projection data set may become inconsistent, in the mathematical sense, after projection-specific filtering. We believe that it is actually more likely that the restoration will make the data more consistent. The advantage of filtering reconstructed images is that a single vector filter is used, ensuring consistency (and speed). However, the noise is no longer white or Poisson in the reconstructed images, and that it is partially correlated pixel-to-pixel [42]. It is thus not clear which approach, projection data or reconstructed image filtering, is best, and further work is warranted.

A comprehensive simulated reconstructed data set would include the effects of scatter, attenuation, depth-dependent blurring, and position-dependent crosstalk. In addition, noise would be simulated as partially correlated pixel-to-pixel and non-Poisson in nature. Here, we have chosen to present preliminary results with a simplified set of simulations, that ignores attenuation and scatter, treats blurring and crosstalk as shift-invariant, and adds uncorrelated Gaussian noise. These simplifications make the simulated data more consistent with the model used to derive and implement the VWF, and may thus give better results than are possible in practice. However, much of the previous work with conventional Wiener filtering, which has yielded useful clinical results, utilized similar simplifications in implementation (e.g., assumption of shift-invariance and white noise). Furthermore, since the point spread functions for the brain simulations were measured in air, we probably underestimated the amount of crosstalk present in a clinical imaging situation. (We measured these in air to be consistent with our pillbox simulations, which also did not model scatter.) Accordingly, we may have underestimated the potential degree of improvement offered by vector Wiener filtering.

Finally, we acknowledge that while Wiener restoration filtering is becoming increasingly popular in nuclear medicine, it is not currently in widespread use. We believe this is due to the need to carefully measure the imaging system's MTF, which a typical user is not able to easily perform. It is also true that least-squares optimization may be appropriate for optimizing quantitative accuracy but not for optimizing diagnostic accuracy of visual interpretation. Thus, a parametric form of the VWF may be useful in some circumstances. In the future, it would be worthwhile to investigate modification of (15) to add an additional adjustment parameter. In this regard, the similarity of (15) to the scalar filter, as shown in Section II-B, should facilitate such an addition.

V. Conclusion

We have described the derivation, implementation, and initial validation of a vector or matrix version of the Wiener filter for use in dual-radionuclide imaging. This filter simultaneously 1) improves contrast in each radionuclide's "direct" image, 2) reduces image noise, and 3) reduces or eliminates the crosstalk contribution from the other radionuclide. We have further analytically and empirically demonstrated that this filter is superior (in the MMSE sense) to the sequential application of separate crosstalk and restoration filters. This filter should prove useful in dual-radionuclide imaging, including those with two emission studies and simultaneous transmission/emission imaging.

Acknowledgment

The authors would like to thank N. Galatsanos for bringing the current literature on multichannel image restoration to their attention and M. Devous for providing the Prism 3000 impulse response functions.

References

[1] G. G. Winzelberg, J. D. Hydovitz, K. R. O'Hara *et al.*, "Parathyroid adenomas evaluated by Tl-201/Tc-99m pertechnetate subtraction scintigraphy and high resolution ultrasonography," *Radiol.*, vol. 155, pp. 231–235, 1985.

[2] T. Mochizuki, T. Takechi, K. Murase, W. N. Tauxe, H. A. Bradfield, S. Tanada, and K. Hamamoto, "Thallium-201/Technetium-99m-phytate (colloid) subtraction imaging of hepatocellular carcinoma," *J. Nucl. Med.*, vol. 35, pp. 1134–1137, 1994.

[3] K. Kawaguchi, T. Sone, H. Tsuboi *et al.*, "Quantitative estimation of infarct size by simultaneous dual radionuclide single photon emission computed tomography: Comparison with peak serum creatine kinase activity," *Amer. Heart J.*, vol. 121, pp. 1353–1360, 1991.

[4] J. Narula, P. D. Nicol, J. F. Southern, P. Pieri, S. M. O'Donnell, J. L. Guererro, N. D. Nossiff, J. B. Newell, H. W. Strauss, and B. A. Khaw, "Evaluation of myocardial infarct size before and after reperfusion: Dual-tracer imaging with radiolabeled antimyosin antibody," *J. Nucl. Med.*, vol. 35, pp. 1076–1085, 1994.

[5] H. Schoeder, H. Topp, M. Friedrich, A. Jatzkewitz, and M. Roser, "Thallium and Indium antimyosin dual-isotope single-photon emission tomography in acute myocardial infarction to identify patients at further ischaemic risk," *Eur. J. Nucl. Med.*, vol. 21, pp. 415–422, 1994.

[6] P. Weinmann, J.-M. Foult, D. Le Guludec, F. Tamgac, D. Rechtman, A. Neuman, N. Caillat-Vigneron, and J.-L. Moretti, "Dual-isotope myocardial imaging: Feasibility, advantages and limitations," *Eur. J. Nucl. Med.*, vol. 21, pp. 212–215, 1994.

[7] H. Weinstein, M. A. King, C. P. Reinhardt, B. A. McSherry, and J. Leppo, "A method of simultaneous dual-radionuclide cardiac imaging with Technetium 99m and Thallium 201. i: Analysis of interradionuclide crossover and validation in phantoms," *J. Nucl. Cardiol*, vol. 1, pp. 39–51, 1994.

[8] M. D. Devous, J. K. Payne, and J. L. Lowe, "Dual-isotope brain SPECT imaging with Technetium-99m and Iodine-123: Clinical validation using xenon-133 SPECT," *Nucl. Med.*, vol. 33, pp. 1919–1924, 1992.

[9] D. L. Bailey, B. F. Hutton, and P. J. Walker, "Improved SPECT using simultaneous emission and transmission tomograph," *J. Nucl. Med.*, vol. 28, pp. 844–851, 1987.

[10] E. C. Frey, B. M. W. Tsui, and J. R. Perry, "Simultaneous acquisition of emission and transmission data for improved Thallium-201 cardiac SPECT imaging using a Technetium-99m transmission source," *J. Nucl. Med.*, vol. 33, pp. 2238–2245, 1992.

[11] M. D. Devous, J. L. Lowe, and J. K. Payne, "Dual-isotope brain SPECT imaging with Technetium and Iodine-123: Validation by phantom studies," *J. Nucl. Med.*, vol. 33, pp. 2030–2035, 1992.

[12] M. Ivanovic, D. A. Weber, S. Loncaric, and D. Franceschi, "Feasibility of dual radionuclide brain imaging with I-123 and Tc-99m," *Med. Phys.*, vol. 21, pp. 667–674, 1994.

[13] H. Kiat, G. Germano, J. Friedman, K. Van Train, G. Silagan, F. P. Wang, J. Maddahi, and D. Berman, "Comparative feasibility of separate or simultaneous rest Thallium-201/stress Technetium-99m-sestamibi dual-isotope myocardial perfusion SPECT," *J. Nucl. Med. 35*, vol. 35, pp. 542–548, 1994.

[14] V. J. Lowe, K. L. Greer, M. W. Hanson, R. J. Jaszczak, and R. E. Coleman, "Cardiac phantom evaluation of simultaneously acquired dual-isotope rest Thallium-201/stress Technetium-99m SPECT images," *J. Nucl. Med.*, vol. 34, pp. 1998–2006, 1993.

[15] E. G. DePuey, "Simultaneous Thallium-201/Technetium-99m dual-isotope cardiac SPECT: Ready for prime time?" *J. Nucl. Med.*, vol. 34, pp. 2006–2008, 1993.

[16] K. Knesaurek, "A new dual-isotope convolution cross-talk correction method: A Tl-201/Tc-99m SPECT cardiac phantom study," *Med. Phys.*, vol. 21, pp. 1577–1583, 1994.

[17] M. A. King, P. W. Doherty, and R. B. Schwinger, "A Wiener filter for nuclear medicine images," *Med. Phys.*, vol. 10, pp. 876–880, 1983.

[18] M. A. King, R. B. Schwinger, P. W. Doherty, and B. C. Penney, "Two-dimensional filtering of SPECT images using the Metz and Wiener filters," *J. Nucl. Med.*, vol. 25, pp. 1234–1240, 1984.

[19] M. A. King, R. B. Schwinger, B. C. Penney, P. W. Doherty, and J. A. Bianco, "Digital restoration of Indium-111 and Iodine-123 SPECT images with optimized Metz filters," *J. Nucl. Med.*, vol. 27, pp. 1327–1336, 1986.

[20] M. A. King, S. J. Glick, B. C. Penney, R. B. Schwinger, and P. W. Doherty, "Interactive visual optimization of SPECT prereconstruction filtering," *J. Nucl. Med.*, vol. 28, pp. 1192–1198, 1987.

[21] M. A. King, B. C. Penney, and S. J. Glick, "An image-dependent Metz filter for nuclear medicine images," *J. Nucl. Med.*, vol. 29, pp. 1980–1989, 1988.

[22] T. R. Miller and K. S. Sampathkumaran, "Design and application of finite impulse response digital filters," *Eur. J. Nucl. Med.*, vol. 7, pp. 22–27, 1982.

[23] ——, "Digital filtering in nuclear medicine," *J. Nucl. Med.*, vol. 23. pp. 66–72, 1982.

[24] T. R. Miller, K. J. Goldman, D. M. Epstein, D. R. Biello, K. S. Sampathkumaran, B. Kumar, and B. A. Siegel, "Improved interpretation of gated cardiac images by use of digital filters," *Radiol.*, vol. 152, pp. 795–800, 1984.

[25] M. T. Madsen and C. H. Park, "Enhancement of SPECT images by Fourier filtering the projection image set," *J. Nucl. Med.*, vol. 26, pp. 395–402, 1985.

[26] J. M. Links, R. W. Jeremy, S. M. Dyer, T. L. Frank, and L. C. Becker, "Wiener filtering improves quantification of regional myocardial perfusion with Thallium-201 SPECT," *J. Nucl. Med.*, vol. 31, pp. 1230–1236, 1990.

[27] J. M. Links, H. L. Loats, P. E. Loats, M. Casey, R. Nutt, and H. N. Wagner, "Simultaneous resolution recovery and noise reduction in positron tomography by Fourier filtering of 2-D projection data," *J. Nucl. Med.*, vol. 31, pp. 862–863, 1990.

[28] J. M. Links, J. P. Leal, H. W. Mueller-Gaertner, and H. N. Wagner, "Improved positron emission tomography quantification by Fourier-based restoration filtering," *Eur. J. Nucl. Med.*, vol. 19, pp. 925–932, 1992.

[29] H. C. Andrews and B. R. Hunt, *Digital Image Restoration*. Englewood Cliffs, NJ: Prentice-Hall, 1977.

[30] R. C. Gonzalez and R. E. Woods, *Digital Image Processing*. New York: Addison-Wesley, 1992.

[31] D. E. Dudgeon and R. M. Mersereau, *Multidimensional Digital Signal Processing*. Englewood Cliffs, NJ: Prentice-Hall, 1984.

[32] B. R. Hunt and O. Kubler, "Karhunen-Loeve multispectral image restoration, Part I: Theory," *IEEE Trans. Acoust., Speech Signal Processing*, vol. ASSP-32, no. 3, pp. 592–600, June 1984.

[33] N. P. Galatsanos and R. T. Chin, "Digital resotration of multichannel images," *IEEE Trans. Acoust., Speech Signal Processing*, vol. 37, no. 3, pp. 415–421, Mar. 1989.

[34] M. K. Ozkan, A. T. Erdem, M. I. Sezan, and A. M. Tekalp, "Efficent multiframe Wiener restoration of blurred and noisy image sequences," *IEEE Trans. Image Processing*, vol. 1, no. 4, pp. 453–476, Oct. 1992.

[35] A. K. Katsaggelos, K. T. Lay, and N. P. Galatsanos, "A general framework for frequency domain multi-channel signal processing," *IEEE Trans. Image Processing*, vol. 2, no. 3, pp. 417–420, July 1993.

[36] T. Kailath, *Lectures on Wiener and Kalman Filtering*. New York: Springer-Verlag, 1981.

[37] E. Wong and B. Hajek, *Stochasic Processes in Engineering Systems*. New York: Springer-Verlag, 1985.

[38] S. M. Kay, *Modern Spectral Estimation: Theory and Application*. Englewood Cliffs, NJ: Prentice-Hall, 1988.

[39] A. V. Oppenheim and R. W. Schafer, *Digital Signal Processing*. Englewood Cliffs, NJ: Prentice-Hall, 1975.

[40] H. W. Muller-Gartner, J. M. Links, J. L. Prince, R. N. Bryan, E. McVeigh, J. P. Leal, C. Davatzikos, and J. J. Frost, "Measurement of radiotracer concentration in brain gray matter using positron emission tomography: MRI-based correction for partial volume effects," *J. Cereb. Blood Flow and Metab.*, vol. 12, pp. 571–583, 1992.

[41] J. M. Links, "Scattered photons as "good counts gone bad," are they reformable, or should they be permanently removed from society?" *J. Nucl. Med.*, vol. 36, pp. 130–132, 1995, Invited Editorial.

[42] R. E. Carson, Y. Yan, M. E. Daube-Witherspoon, N. Freedman, S. L. Bacharach, and P. Herscovitch, "An approximation formula for the variance of PET region-of-interest values," *IEEE Trans. Med. Imag.*, vol. 12, pp. 240–250, 1993.